Motion-based Separation and Imaging of Closely-Spaced Extended Targets

Xu, Shengzhi; Yarovoy, Alexander

DOI
10.1109/JSEN.2020.3004909

Publication date
2020

Document Version
Final published version

Published in
IEEE Sensors Journal

Motion-Based Separation and Imaging of Closely Spaced Extended Targets

Shengzhi Xu and Alexander Yarovoy, *Fellow, IEEE*

***Abstract*—Separating images of multiple moving extended-targets by means of ultra-wideband (UWB) frequency-modulated-continuous-wave (FMCW) radar is investigated. The difference in motion of closely-spaced extended targets is used to separate and image them when their radar signatures overlap in the range-azimuth domain. A novel auto-focusing criterion based on the entropy of the eigenspectrum and the Fourier spectrum is proposed for target imaging using inverse synthetic aperture radar (ISAR). It allows separating closely spaced targets and estimating their motion parameters. The criterion proposed overcomes the low Doppler resolution of closely-spaced extended targets of conventional techniques. The bearing information is extracted by signal reconstruction for every target separately. With the estimated position and the motion parameters of multiple targets, their images are reconstructed using standard imaging processing algorithms. The performance of the proposed method is validated via numerical simulations.**

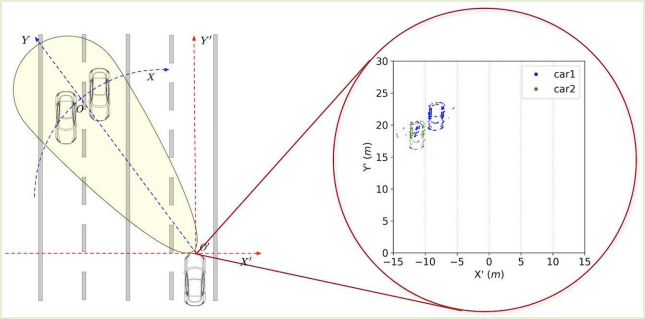

***Index Terms*— Frequency modulated continuous wave (FMCW), inverse synthetic aperture radar (ISAR), eigenspectrum, ultra-wideband (UWB).**

I. Introduction

THE separation of multiple closely-spaced moving targets and the estimation of their positions and motions parameters are important for numerous civil and military applications. The motion information can be used for target separation in the case when targets cannot be separated in range and azimuth. In an example shown in Fig. 1, responses of both cars at the left lanes overlap in the range-azimuth output of a typical automotive radar with a typical resolution in azimuth of about 10 degrees for 3 transmit and 4 receive antennas. To observe the motion differences, the observation time is extended to increase the Doppler resolution. The differences between the Doppler shifts of strong scatterers from the same target will be observed when the Doppler resolution is sufficiently high. This phenomenon is used to image the targets and is called ISAR imaging [1]. ISAR imaging of a single target has been thoroughly studied and is widely used for target classification and recognition [2]. One of the key techniques for ISAR imaging is the range alignment by motion compensation. Many algorithms have been proposed for motion parameters estimation, such as the centroid tracking algorithm [3], the entropy minimisation (EM) [4], the phase gradient auto-focusing technique [5], the image contrast maximisation [6]. Among them, EM is one of the most popular and widely used methods. Moreover, many improved algorithms based on EM have been introduced, such as Rényi

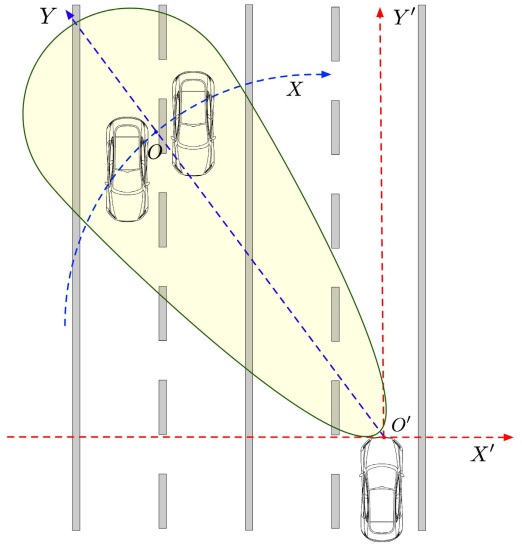

Fig. 1. Traffic scenario where two cars cannot be separated in either beam or range profile.

Manuscript received January 21, 2020; revised June 8, 2020; accepted June 10, 2020. Date of publication June 25, 2020; date of current version October 16, 2020. The associate editor coordinating the review of this article and approving it for publication was Dr. Michael Antoniou. *(Corresponding author: Shengzhi Xu.)*

The authors are with the Department of Microwave Sensing, Signals, and Systems, Delft University of Technology, 2628 CD Delft, The Netherlands (e-mail: s.xu-4@tudelft.nl).

Digital Object Identifier 10.1109/JSEN.2020.3004909

entropy [7], Tsallis entropy [8] and efficient implementation of EM [9], [10].

In the case of multiple targets presented in the observed scene, the conventional methods of range alignment and phase adjustment proposed for the only single target may fail to image the targets. Therefore, many algorithms are proposed to separate and image multiple targets. Current approaches of multiple targets separation in ISAR imaging can be roughly categorised into two categories: direct imaging [1], [11], [12] and separated imaging [13]–[22].

If the targets are far-spaced, a coarse image of the targets can be obtained and the targets can be separated in the coarse image using imaging segmentation techniques [1], [11] or sparse representation [12] and more precise images can be achieved by accurate motion compensation separately.

An alternative situation, when the range histories of the targets are overlapped, is much more challenging. For such cases, several popular types of algorithms are intensively studied. One is based on time-frequency (TF) analysis which is used to separate different sources in TF domain [13]–[16]. However, there are crucial limitations for the use of TF analysis: Wigner-Ville distribution(WVD) and Radon-Wigner transform (RWT) suffer from cross-terms, and short-time Fourier transform (STFT) has a poor frequency resolution. Another well-known algorithm uses fractional Fourier transform (FrFT) [17] to extract the higher-order phase terms of the signal which are related to the acceleration and jerk. However, the closely-spaced targets with the same or similar acceleration are difficult to be recognised by FrFT. Several lines or curves detection based algorithms [18], [19], such as Hough Transform, are applied to separate the range profile of each target. However, the performance of these algorithms decreases significantly when the range histories of different targets are seriously overlapped. Another approach is the exhaustive search of the motion parameters and using auto-focusing criteria as the indications to estimate these parameters [20], [21]. Based on the auto-focusing approach, many algorithms are introduced to separate and image multiple moving targets, e.g., the Modified Keystone [17], [22] and Radon-Transform [23].

Although the previous Fourier spectrum-based auto-focusing criteria [11], [20], [21] are quite sensitive to the differences of the higher-order motion parameters (acceleration and jerk), they are much less affected by the Doppler differences. Such low sensitivity leads to a poor separation in velocity. To overcome such a drawback, a novel criterion based on the entropy of the eigenspectrum is proposed in this paper to separate targets with high Doppler velocity resolution. Since the eigenspectrum has a much higher sensitivity to the second-order mutual coupling introduced by the constant Doppler shifts, targets with similar radial velocities can be separated in the eigenspectrum-based EM but may not be separated by the conventional Fourier spectrum-based EM. The proposed criterion has, however, a low resolution and spread entropy information for higher-order motion parameters such as acceleration. Therefore, a simple method to combine both entropies is introduced, resulting in high resolutions for both velocities and accelerations. After estimating the motion parameters, the targets are imaged and separated by different range history alignments. Then, based on the image and estimated parameters, the signal models of each target are reconstructed. The matched filter is applied to estimate the corresponding azimuths using the reconstructed signal model of each target separately. At last, the observed scene of multiple targets will be imaged based on the estimated parameters.

Notations used in this paper are as follows. Scalars are denoted by lower-case letters, vectors and matrices are written as lower-case and upper-case bold-face letters, and multi-way tensors are written as bold-face calligraphic letters respectively. $(\cdot)^T$, $(\cdot)^H$ and $(\cdot)^*$ denote the transpose, conjugate transpose and complex conjugate of a vector or matrix, respectively. Symbols $\odot$ and $\circ$ represent the Hadamard product and outer product, respectively. $\lfloor x \rfloor$ gives the nearest integer less than or equal to x. The $\mathcal{O}$ is the asymptotic notation. The notation $\boldsymbol{\sigma}(\mathbf{A})$ denotes the spectrum of the matrix $\mathbf{A}$; $[\mathbf{A}]_{p,q}$ denotes the entry of matrix $\mathbf{A}$ at the $(p+1)$th row and $(q+1)$th column. This means the indices of the vector, matrix and tensor in this paper are starting from 0. $\mathrm{Tr}(\mathbf{A})$ returns the trace of matrix $\mathbf{A}$. $\mathbf{vec}(\mathbf{A})$ yields the vector of stacking the $\mathbf{A}$'s columns together [24]. $\mathcal{F}()$ represents the full-dimensional fast Fourier transform (FFT) operation. A special vector $\mathbf{1}_M$ is defined as $\mathbf{1}_M = [1, 1, \ldots, 1] \in \mathbb{R}^M$. $||\boldsymbol{\mathcal{A}}||$ returns the norm of the tensor $\boldsymbol{\mathcal{A}}$ [25].

The rest of the paper is organised as follows. The signal model for multiple extended-targets illuminated by FMCW signals is established in Section II. A new criterion for auto-focusing ISAR imaging is introduced in Section III. Numerical simulations are presented in Section IV and the conclusions are drawn in Section V.

II. Signal Model

In this section, the signal model of multiple extended targets using wideband FMCW is formulated. Assume that I moving targets represented by J dominant scatterers are presented in the observed domain and illuminated by the radar [26]. A sequence of chirps are transmitted with the normalised single chirp form as

$$s_0(t) = e^{j2\pi(f_0 t + 0.5\mu t^2)} \quad t \in [0, T_0], \tag{1}$$

where f_0 is the starting frequency, T_0 is the chirp duration interval, the time $t \in (T_0, T)$ is the system reset interval and T is the sweep repetition interval, and $\mu = \dfrac{B}{T_0}$ denotes the frequency modulation rate. The periodic transmitted signal is decomposed into fast-time domain t' and chirp number (slow-time) domain $t_m = mT$ as $t' = t - t_m$, $t' \in [0, T)$, where $m = \left\lfloor \dfrac{t}{T} \right\rfloor$, $m = 0, 1, 2, \ldots, M-1$ and M is the total number of the chirps in one coherent processing interval (CPI). Then the periodically transmitted signal is decomposed in terms of fast-time t' and slow-time t_m as

$$s(t) = s(t' + t_m) = s(t_m, t') = s_0(t'). \tag{2}$$

Since the scatterers from one target could have different velocity projection on the line of sight (LOS) and the corresponding received signals contain different Doppler information as well, a scattering centroid is chosen as a reference phase centre. Generally, the scattering centre can be chosen randomly close to the geometric centroid of the target. Consequently, the scattering centre is usually not unique but located in a bounded region (acceptable boundaries). The acceptable boundaries indicate the minimum Doppler domain in the expanded range-Doppler map (with different fold numbers), within which all the scatterers of one target are included. It is assumed that the instantaneous range of the ith scattering centre is expressed as the second-order polynomial

$$R_i(t_m) = R_{i0} + v_i t_m + \frac{1}{2} a_i t_m^2, \tag{3}$$

where R_{i0} denotes the initial range of the scattering centre of the ith target ($i = 1, 2, \ldots I$) and the corresponding motion parameters, velocity and acceleration are denoted by v_i and a_i, respectively. Here, the fast-time t' is directly omitted since $t' \ll t_m$. Moreover, the higher-order motion parameters are ignored since it is sufficiently accurate to describe the movements of the targets with the second-order Taylor polynomial in a short time [22], [27]. It is worth noting that, the proposed algorithm would also work for higher-order motions at the price of an increased computational burden.

The instantaneous range of the jth scatterer ($j = 1, 2, \ldots, J$) includes the polynomial term $R_i(t_m)$ and the triangular terms which denote the relative range to the phase centre and the projection of the cross-range on the LOS. Therefore, the instantaneous range of the jth scatterer of ith target is given as [2], [15]

$$\begin{aligned} R_{ij}(t_m) &= R_i(t_m) + y_{ij}\cos(\omega_i t_m) + x_{ij}\sin(\omega_i t_m) \\ &\approx R_{i0} + v_i t_m + \frac{1}{2} a_i t_m^2 + y_{ij} + x_{ij}\omega_i t_m, \end{aligned} \tag{4}$$

where y_{ij} and x_{ij} denote range and cross-range relative to the scattering centre of jth scatterer of ith target, ω_i is the rotational speed of ith target, which is provided by the tangential velocity. Since the observation time is short, the assumptions $\cos(\omega_i t_m) \approx 1$ and $\sin(\omega_i t_m) \approx \omega_i t_m$ are made to linearise the model [2], [15].

Then the round trip delay of the transmitted waves reflected from the jth scatterer of ith target is then written as

$$\tau_{ij}(t_m) = \frac{2R_{ij}(t_m)}{c}, \tag{5}$$

where c is the speed of the light.

Insert (4) in (5), the round-trip delay is written as

$$\begin{aligned} \tau_{ij}(t_m) &= \frac{2R_{ij}(t_m)}{c} \\ &= \frac{2}{c}\left(R_{i0} + v_i t_m + \frac{1}{2} a_i t_m^2 + y_{ij} + x_{ij}\omega_i t_m \right) \\ &= \frac{2(R_{i0} + y_{ij})}{c} + \frac{2(v_i + x_{ij}\omega_i)}{c} t_m + \frac{a_i}{c} t_m^2. \end{aligned} \tag{6}$$

By choosing a proper scattering centre, the target "*shape*" could be constructed by y_{ij} and $x_{ij}\omega_i$. Here, the "*shape*" is a distorted shape in the range-crossrange plane, and if the ω_i can be correctly estimated, the real range-crossrange shape can be reconstructed.

With the time delay in (6), the received wave of jth scatterer from ith target is obtained as $r_{ij}(t) = \alpha_{ij} s(t - \tau_{ij}(t_m))$. Then $r_{ij}(t)$ is mixed with the conjugate copy of the transmitted wave and the de-chirped signal of such scatterer is obtained as

$$\begin{aligned} y_i(t_m, t') &= r_{ij}(t_m, t') s^*(t_m, t') \\ &= \alpha_{ij} \exp\{ j2\pi [f_0(t' - \tau_{ij}(t_m)) + \mu(t' - \tau_{ij}(t_m))^2 \\ &\quad - f_0 t' - \mu t'^2]\} \\ &\approx \alpha_{ij} \exp[-j2\pi (f_0 \tau_{ij}(t_m) + 2\mu \tau_{ij}(t_m) t')] \\ &= \alpha_{ij} \exp\Big\{ -j2\pi \Big[f_0 \frac{2(v_i + x_{ij}\omega_i)}{c} t_m \\ &\quad + f_0 \frac{a_i}{c} t_m^2 + 2\mu \frac{2(R_{i0} + y_{ij})}{c} t' \\ &\quad + 2\mu \frac{2(v_i + x_{ij}\omega_i)}{c} t_m t' + 2\mu \frac{a_i}{c} t_m^2 t' \Big] \Big\}, \end{aligned} \tag{7}$$

where α_{ij} is the complex amplitude of jth scatterer of ith target, and the constant terms $\exp\left(-j4\pi f_0 \frac{R_{i0} + y_{ij}}{c} \right)$ and $\exp\left[4\mu \left(\frac{R_{i0} + y_{ij}}{c} \right)^2 \right]$ are subsumed into the constant amplitudes term α_{ij}. Here since the observing time is very short, we assume that the amplitudes of all the scatterers do not change within one CPI.

Sampling the data $y_i(t_m, t')$ in terms of the fast-time t' with frequency f_s (sampling interval $T_s = \frac{1}{f_s}$), the data can be stacked in matrix form $\mathbf{X}_i \in \mathbb{C}^{M \times K}$

$$\begin{aligned} \mathbf{X}_{ij} = \alpha_{ij} \mathbf{f}_d(v_i + x_{ij}\omega_i) \mathbf{f}_r^T(y_{ij}) \\ \odot \Psi(v_i + x_{ij}\omega_i) \odot \mathbf{\Omega}(a_i) \odot \Theta(a_i), \end{aligned} \tag{8}$$

where $k = 0, 1, \ldots, K-1$ is the fast-time sampling indices and K is the total samples in one chirp, and the sinusoidal vectors $\mathbf{f}_d(v_i + x_{ij}\omega_i) \in \mathbb{C}^{M \times 1}$, $\mathbf{f}_r(y_{ij}) \in \mathbb{C}^{K \times 1}$ are

$$\begin{aligned} \mathbf{f}_d(v_i + x_{ij}\omega_i) &= \Big[1, \exp\big(-j4\pi \frac{v_i + x_{ij}\omega_i}{\lambda} T \big), \ldots, \\ &\qquad \exp\big(-j4\pi \frac{v_i + x_{ij}\omega_i}{\lambda} T(M-1) \big) \Big]^T, \\ \mathbf{f}_r(y_{ij}) &= \Big[1, \exp\big(-j8\pi\mu \frac{R_{i0} + y_{ij}}{c f_s} \big), \ldots, \\ &\qquad \exp\big(-j8\pi\mu \frac{R_{i0} + y_{ij}}{c f_s} (K-1) \big) \Big]^T, \end{aligned} \tag{9}$$

where $\lambda = \frac{c}{f_0}$ is the wavelength corresponding to the lowest frequency of the band, and the coupling matrices $\Psi(v_i + x_{ij}) \in \mathbb{C}^{M \times K}$, $\mathbf{\Omega}(a_i) \in \mathbb{C}^{M \times K}$, $\Theta(a_i) \in \mathbb{C}^{M \times K}$ are defined with entries as

$$\begin{aligned} [\Psi(v_i + x_{ij})]_{m,k} &= \exp\Big[-j8\pi\mu \frac{v_i + x_{ij}\omega_i}{c f_s} T m k \Big], \\ [\mathbf{\Omega}(a_i)]_{m,k} &= \exp\Big[-j2\pi f_0 \frac{a_i}{c} T^2 m^2 \Big], \\ [\Theta(a_i)]_{m,k} &= \exp\Big[-j4\pi\mu \frac{a_i}{c f_s} T^2 m^2 k \Big]. \end{aligned} \tag{10}$$

The signal model for a single scatterer contains the sinusoidal terms $\mathbf{f}_d(v_i + x_{ij}\omega_i)$ and $\mathbf{f}_r(y_{ij})$, whose Fourier spectrum reveals the distorted shape of the targets by y_{ij} and $x_{ij}\omega_i$.

In addition to the sinusoidal terms, there are three extra coupling components. The second-order mutual coupling term $\Psi(v_i + x_{ij}\omega_i)$ is the function of the Doppler velocity v_i which contains in $v_i + x_{ij}\omega_i$. Here, the velocity v_i can be larger than the maximum unambiguous velocity of the system and will be folded in the unambiguous Doppler interval. This is one of the main problems for target detection and parameter estimation in most cases when the acceleration of the target is ignored. The high-order phase term $\Omega(a_i)$ and higher-order asymmetric mutual coupling term $\Theta(a_i)$ contain the higher-order motion parameters, i.e. the acceleration a_i. To image the ith target in the range-Doppler map, all these coupling terms should be correctly compensated.

The matrix data of a single antenna element are $\mathbf{X}_{ij}$. Now the uniformly distributed linear antenna array (ULA) for receiver is considered and the wideband steering matrix $\mathbf{A}(\theta_{ij}(t_m)) \in \mathbb{C}^{L\times K}$ can be written as [28]

$$\mathbf{A}(\theta_{ij}(t_m)) = \mathbf{a}(\theta_{ij}(t_m))\mathbf{1}_k^T \odot \mathbf{\Phi}(\theta_{ij}(t_m)), \tag{11}$$

where $\theta_{ij}(t_m)$ is the azimuth of the jth scatterer of the ith target at the time t_m and the narrowband steering vector is

$$\mathbf{a}(\theta_{ij}(t_m)) = \Big[1, \exp\big(-j2\pi\frac{d}{\lambda}\sin(\theta_{ij}(t_m))\big), \ldots, \exp\big(-j2\pi\frac{(L-1)d}{\lambda}\sin(\theta_{ij}(t_m))\big)\Big]^T, \tag{12}$$

and the coupling term introduced by the wideband waveform is adopted from [28] as

$$[\mathbf{\Phi}(\theta_{ij}(t_m))]_{l,k} = \exp\Big(-2j\pi\mu\frac{lkd}{cf_s}\sin(\theta_{ij}(t_m))\Big). \tag{13}$$

Stacking all the slow-time t_0 to t_{M-1} forms the tensor data $\mathcal{A}_{ij} \in \mathbb{C}^{M\times K\times L}$ as

$$\mathcal{A}_{ij} = \begin{array}{c}\mathbf{A}(\theta_{ij}(t_0))\\ \mathbf{A}(\theta_{ij}(t_1))\\ \vdots \\ \mathbf{A}(\theta_{ij}(t_{M-1}))\end{array}. \tag{14}$$

Now the discretised data $\mathcal{Y}_{ij} \in \mathbb{C}^{M\times K\times L}$ of the antenna array of the jth scatterer of ith target are stacked as a tensor, given by

$$\mathcal{Y}_{ij} = \mathcal{A}_{ij} \odot (\mathbf{X}_{ij} \circ \mathbf{1}_L), \tag{15}$$

and the received multi-way data $\mathcal{Z} \in \mathbb{C}^{M\times K\times L}$ in the presence of the noise are written as

$$\mathcal{Z} = \sum_{i=1}^{I}\sum_{j=1}^{J}\mathcal{Y}_{ij} + \mathcal{N}, \tag{16}$$

where $\mathcal{N}$ is the discrete multi-way additive complex Gaussian white noise with the entries' distribution as $\mathcal{N}(0, \sigma^2)$.

Now the problem is to estimate the motion parameters and image the targets from the tensor data $\mathcal{Z}$.

III. Motion-Based Target Separation and Imaging

In this section, we propose a novel method for multiple closely-spaced extended targets separation and imaging. Firstly, the motion parameters of the targets are estimated using the combination of the conventional Fourier spectrum-based entropy and the proposed eigenspectrum-based entropy. Secondly, the ISAR imaging is performed via the range-Doppler processing and a simple thresholding method is applied to separate multiple targets. Thirdly, the azimuths of the targets are estimated accordingly using the signal reconstruction of the targets. Finally, the observed scene is reconstructed via an image processing technique using the estimated target motion parameters.

A. Motion Parameters Estimation

To present the 2D targets in the Fourier spectrum using the conventional range-Doppler algorithm, the range migration needs to be eliminated. To align the range history, or equivalently to compensate the coupling components $\Psi(v_i + x_{ij}\omega_i)$, $\Omega(a_i)$ and $\Theta(a_i)$, the motion parameters of the scattering centre v_i and a_i should be estimated. However, since the motion parameters of targets are usually different, the range alignments of all the observed targets cannot be performed simultaneously. The Shannon Entropy of the Fourier spectrum provides an efficient way of estimating the motion parameters for a single extended target and can be applied in the multi-targets scenario if the targets have sufficiently different motion parameters [4], [10], [27]. The Shannon entropy for a vector $\mathbf{s} = [s_1, \ldots, s_N]$ with positive entries is defined by

$$\text{Entropy}(\mathbf{s}) = -\sum_{n=1}^{n=N} p_n \log p_n, \tag{17}$$

where

$$p_n = \frac{s_n}{\sum_n s_n}. \tag{18}$$

According to the definition of the Shannon entropy, when the targets are correctly focused by motion compensation, the FFT result yields a minimum entropy value. In terms of velocity v and acceleration a, the range alignment is performed via phase compensation as

$$\begin{aligned}\hat{\mathbf{Y}}(v,a) &= \mathbf{Y} \odot \Psi^*(v) \odot \mathbf{\Omega}^*(a) \odot \Theta^*(a)\\ &= \alpha_{ij}\mathbf{f}_d(v_i + x_{ij}\omega_i)\mathbf{f}_r^T(y_{ij})\\ &\quad \odot \Psi(v_i - v + x_{ij}\omega_i)\\ &\quad \odot \mathbf{\Omega}(a_i - a) \odot \Theta(a_i - a),\end{aligned} \tag{19}$$

where $\mathbf{Y} = [\mathcal{Z}]_{:,:,0}$ is the data of the first antenna element. With the power spectrum $\mathbf{P}(v,a) = (\mathcal{F}\hat{\mathbf{Y}}(v,a)) \odot (\mathcal{F}\hat{\mathbf{Y}}(v,a))^*$, the motion parameters are estimated via the optimisation:

$$\tilde{v}, \tilde{a} = \underset{v,a}{\text{argmin}}\ \text{Entropy}[\mathbf{vec}(\mathbf{P}(v,a))]. \tag{20}$$

The conventional Fourier spectrum-based Shannon entropy works properly when the motion parameters of different targets - velocities or accelerations - are significantly distinct. However, the Fourier spectrum has relatively low sensitivity on

the second-order mutual coupling, therefore, it may be difficult to separate the targets when they are moving with slightly different velocities and similar acceleration.

To overcome this problem, we propose a novel approach based on Shannon entropy of the matrix eigenspectrum for motion parameters estimation given by

$$\begin{aligned}\mathbf{R}(\upsilon, a) &= \hat{\mathbf{Y}}(\upsilon, a)\hat{\mathbf{Y}}^H(\upsilon, a),\\ \tilde{\upsilon}, \tilde{a} &= \underset{\upsilon, a}{\operatorname{argmin}}\ \text{Entropy}[\boldsymbol{\sigma}(\mathbf{R}(\upsilon, a))].\end{aligned} \tag{21}$$

It is worth noting that $\mathbf{R}(\upsilon, a) = \hat{\mathbf{Y}}^H(\upsilon, a)\hat{\mathbf{Y}}(\upsilon, a)$ can also be used for EM. Moreover, since the eigenspectrum is insensitive to the auto-coupling terms, the $\hat{\mathbf{Y}}(\upsilon, a)$ can be replaced by $\hat{\mathbf{Y}}(\upsilon, a) = \mathbf{Y} \odot \Psi^*(\upsilon) \odot \Omega^*(a)$, where the term $\Theta^*(a)$ is omitted for computational simplicity. The proposed approach is based on the fact that the off-grid eigenspectrum has a much higher sensitivity to the second-order mutual coupling terms than the grid-based Fourier spectrum and has no side-lobes issues.

Although the proposed entropy has higher velocity resolution, it is much less affected by the coupling terms $\Theta(a_i)$ and $\Omega(a_i)$. This is because these coupling terms have much less influence on the orthogonality of the eigenvectors. Therefore, it is possible to have two entropy maps together, where the Fourier spectrum-based entropy has a higher resolution for the higher-order motion parameters, while eigenspectrum-based entropy has a higher resolution for the first-order motion parameters. A straightforward approach is to combine these two entropies to obtain high-resolution separation both on velocity and acceleration.

Before combining them, the entropy maps should be normalised into the same scale. We propose to use the normalisation towards the interval [0, 1] by

$$N(I) = \frac{I - \min(I)}{\max(I) - \min(I)}, \tag{22}$$

where I denotes the entropy map constructed by the entropy value of all the points in the searching grid of velocity and acceleration, and max() and min() return the maximum and minimum value of the map. To benefit from the high sensitivities to different motion parameters, we propose the novel metric obtained from both entropy maps:

$$S = 1 - [1 - N(F)][1 - N(\Sigma)], \tag{23}$$

where F and Σ are the entropy maps of Fourier spectrum and eigenspectrum, respectively. Then the motion parameters can be estimated by finding the local minima of the combined entropy map of S.

To automatically detect the targets and estimate the motion parameters, some further steps should be performed. Since both entropy maps contain noise, there might be many local minima introduced by the noise. To alleviate the influence of noise, the total variation (TV) denoising algorithm [29] is applied to the combined entropy. This processing removes most of the local minima. The locations of the local minima would indicate the motion parameters of the targets.

B. Target Imaging and Separation

With the estimated parameters from the previous step, the targets can be imaged separately by appropriate range alignments. Through the coupling terms compensation for the scattering centre, most of the signal distortion due to the range migration will be eliminated. However, that is not sufficient to obtain a well-focused image due to the Doppler differences of the scatterers to the phase centre. The Keystone transform is performed to the aligned data within the maximum unambiguous Doppler interval [22]. The process is illustrated as

$$\begin{aligned}\mathcal{F}\{\text{Keystone}[\mathbf{Y} \odot \Psi^*(\tilde{\upsilon}) \odot \Omega^*(\tilde{a})\\ \odot\Theta^*(\tilde{a}) \odot (\mathbf{f}_d(\tilde{\upsilon})\mathbf{1}_K^T)^*]\},\end{aligned} \tag{24}$$

where Keystone denotes the Keystone transform operation and the term $(\mathbf{f}_d(\tilde{\upsilon})\mathbf{1}_K^T)^*$ is used to put the scattering centre in the centroid of the spectrum. If the estimation results are located within the acceptable boundary, all the scatterers of one target are shifted into the observation window without Doppler ambiguity, and the FFT and Keystone transform will generate a focused image.

Here we also assume that the targets would not be focused at the same time; otherwise, they will be recognised as the same target. According to this assumption, when one target is focused, the others would not be entirely focused. Then, the multiple targets can be separated with the CLEAN techniques or the thresholding method [20]. If the targets are constructed of too many scatterers, it is time-consuming to apply the CLEAN technique, therefore, the simpler thresholding is adopted in this paper for target detection and separation. From the separated focused range-Doppler map, the distorted shape of the targets can be recognised and parameters of all the dominant scatterers $\tilde{y}_{ij}$ and $\tilde{x}_{ij}\tilde{\omega}_i$ are estimated.

C. Azimuthal Beamforming

Multiple targets may not be separable in the azimuthal domain by means of traditional beamforming techniques if they are closely positioned or even partially overlapped. Although the subspace-based methods can provide super-resolution ability, most of them are applicable only for point-like targets and not suitable for extended targets considered in this study [28]. Fortunately, since the targets have been separated from the previous steps, the corresponding azimuthal information can be estimated.

Because the azimuthal values of the targets are slightly changing with time, to accurately estimate them, the data $\mathbf{Z} = [\boldsymbol{\mathcal{Z}}]_{0,:,:}$ of the first slow-time index are used to avoid angle migration.

To estimate the azimuth of a single target, we apply beam-forming with the reconstructed data of each target separately. For the ith target, the reconstructed data for the first slow-time sample and the searching angle grid θ are

$$\tilde{\mathbf{Z}}_i(\theta) = \mathbf{A}(\theta) \odot \Big(\sum_{j=1}^{J} \tilde{\alpha}_{ij}\mathbf{1}_M\mathbf{f}_r^T(\tilde{y}_{ij})\Big). \tag{25}$$

Then the estimation can be made simply by

$$\tilde{\theta}_i = \underset{\theta}{\operatorname{argmax}}\ |\text{Tr}[\tilde{\mathbf{Z}}_i^H(\theta)\mathbf{Z}]|. \tag{26}$$

D. Imaging of the Observed Scene

According to the parameters estimated above, we can image the observed scene of multiple moving targets. Here, we assume the ranges of the targets are known, which are easily estimated from the range profile and we also assume that all the targets move along the Y' axis. Then, the image of the observed scene can be obtained by a few steps:

1) Image Rescaling: Since the images are distorted by the $x_{ij}\omega_i$, the real crossrange x_{ij} is rescaled by dividing the ω_i, where $\omega_i \approx \dfrac{v_i \tan\theta_i}{R_{i0}}$.

2) Rotation and Location: The range-crossrange map is transformed to real geometric coordinates $X'OY'$ according to the angle θ_i for the ith target separately. Finally, based on the estimated positions of the centroid of the targets θ_i and R_i, the focused images of all the targets are placed in the corresponding positions.

IV. Simulations

In this section, the simulation results are presented to demonstrate the performance of the proposed algorithm and further discussions are also provided.

A. Numerical Simulations

The automotive scenario is considered and the radar has the following parameters. The bandwidth of FMCW signal is $B = 4$ GHz with starting frequency $f_0 = 77$ GHz, the chirp duration is $T_0 = 320$ μs and the chirp repetition interval is $T = 400$ μs. $M = 156$ chirps are transmitted in a burst and the reflected signals are received by the ULA with $L = 8$ antenna elements. After the de-chirping process, the data are sampled with the sampling frequency of $f_s = 625$ kHz. Then the received data in the multi-way form $\boldsymbol{\mathcal{Z}} \in \mathbb{C}^{156\times200\times8}$ are used to estimate the motion parameters. To demonstrate imaging capabilities of the method each car model is represented by 137 point scatterers which are generated randomly from the edges of the car as shown in Fig. 2 according to the Swerling model [26]. The data set is inspired by the data dome [30] and the measurements presented in [31]. Despite being placed around positions of strong physical scatterers at a car body, these point scatterers are not meant to fully mimic physical scattering from a car. These scatterers are also assumed to be isotropic and provide constant amplitude and phase of the scattered field during the processing period (60 ms), similar to the approach in [31]. To simplify numerical analysis later but without restricting the generality of the imaging approach proposed, we shall not consider possible multipath propagation of electromagnetic waves due to reflection from the road. The multi-path propagation of electromagnetic waves due to reflections from the road will influence the received signal, which may result in the appearance of additional points in the image when the specular reflection from the road surface is sufficiently strong (very smooth road surface, water layer above the road, etc.).

The amplitudes of all the scatterers are set from uniform distribution $\alpha_{ij} \sim \mathcal{U}(0.8, 1)$. The signal-to-noise ratio (SNR) is set to $\mathrm{SNR} = 10\log_{10}\dfrac{||\sum_{i=1}^{I}\sum_{j=1}^{J}\boldsymbol{\mathcal{Y}}_{ij}||^2}{||\boldsymbol{\mathcal{N}}||^2} = 10$ dB with additive complex Gaussian noise.

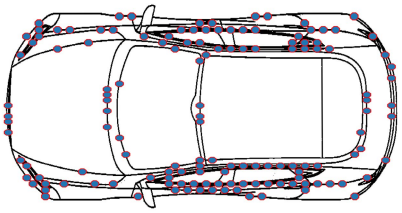

Fig. 2. Car model with 137 point scatters.

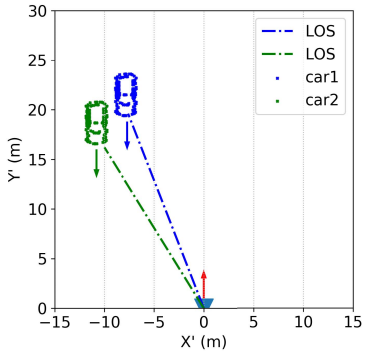

Fig. 3. The geometry of the simulations.

To validate the performance of separating multiple closely-spaced targets, two cars are set in the observed domain, which cannot be separated from the beam and range profile. The exact geometry of the two cars is shown in Fig. 3, where the radar is located in the position of $(0, 0)$. This scenario is very common in the real world, where two cars are close to each other and partially overlapped with each other in both beam and range. It is worth noting that the real geometry is indicated by axis X' and Y', while the ranges X of the LOS are indicated by the dashed lines. The velocities of car1 and car2 are set as 20.87 m/s and 20.62 m/s along the negative Y' axis. We assume the radar is mounted on the vehicle which has a velocity of 19.44 m/s along the positive Y' axis. Thus, the total relative velocities of the cars to the radar are -40.31 m/s and -40.06 m/s along the Y-axis and the velocity projections of the scattering centre of the targets on the LOS are -37.89 m/s and -34.69 m/s, respectively. Moreover, the accelerations of both targets are set to $a_i = 0$ to test the capability of separating two cars from the Doppler differences.

According to the parameter setting of the system and the objects, the discrete received data in tensor form are established using the signal model (16). It is worth noting that in reality, only half of these scatterers can be illuminated by the radar due to the propagation of the radio wave, but for simulation, we assume all these scatterers are observed by the radar. In the signal model, the relative velocities of the cars along the Y' axis are divided into two orthogonal components, the radial parts $v_{\parallel}$ in the direction to the radar and tangential parts $v_{\perp}$ which is orthogonal to the radial parts $v_{\parallel}$ and provide the rotational speeds of the targets as $\omega = \dfrac{v_{\perp}}{R}$. Here, since the observing time is very short and

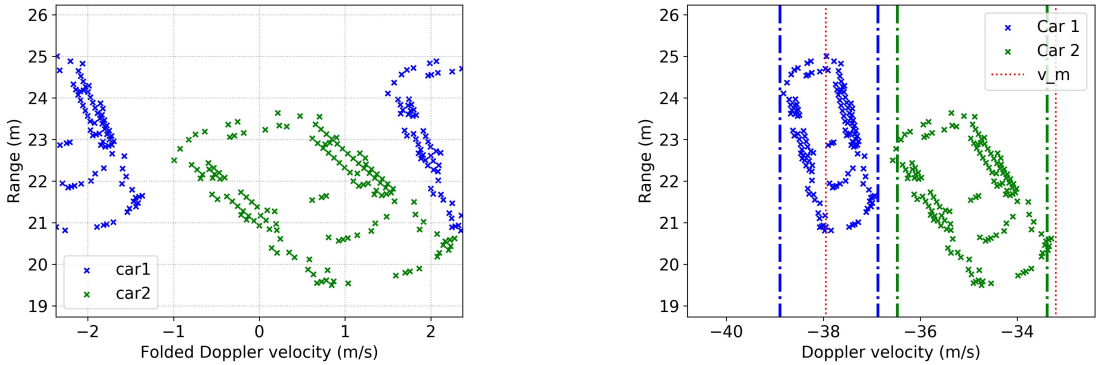

Fig. 4. Range-Doppler map for (a) range-Doppler map in the observed window and (b) unfolded range-Doppler map.

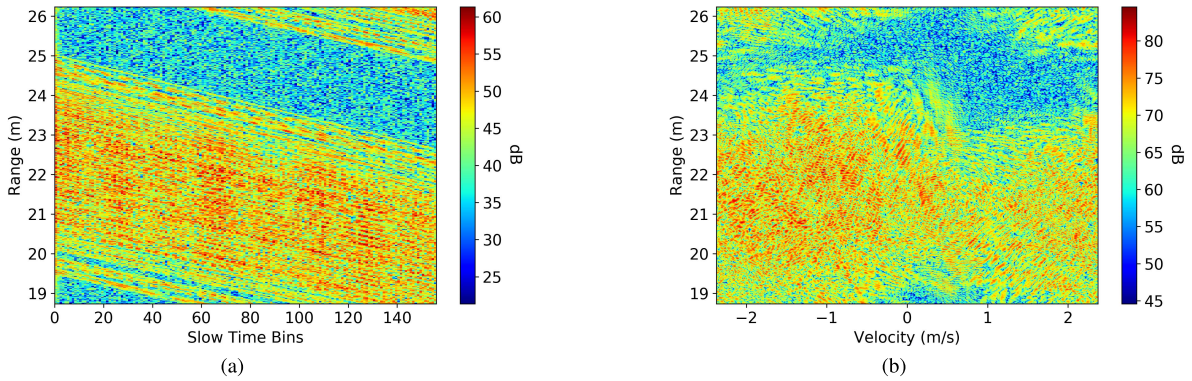

Fig. 5. (a) 1D FFT on fast-time to show the range migration with slow-time bins and (b) 2D FFT imaging result without motion compensation.

the rotational acceleration is usually small, we assume the speeds are constant over one CPI. In fact, this assumption is also not necessary since the rotational acceleration can also be compensated using well-known approaches, but this is not the main contribution in our paper, so in order to keep the focus of the manuscript on the main novelty we assume constant rotational speed during the CPI.

For comparison, the ideal imaging results of all the scatterers without any coupling components are shown in Fig. 4. Fig. 4(a) shows the positions of the scatterers of the cars in the observed window, where the observed window means the unambiguous range-Doppler map with 0 fold number. Fig. 4(b) illustrates the corresponding unfolded imaging results with the green and blue dashed lines indicating the region of acceptable boundaries of two cars and the space between the red dashed lines indicates the maximum unambiguous domain. All the velocity estimations within the dashed lines would compensate most of the coupling influence and bring the target close to the centroid of the observed window. One of the main objectives in the following simulation is the estimation of the motion parameters of the cars and reconstruction of the unfolded range-Doppler map similar to Fig. 4(b).

By applying 1D FFT on the fast-time domain of the data, the range migration phenomenon of two cars is shown in Fig. 5(a), in which the range histories of two targets are overlapped with the same slope and are hardly separated. Fig. 5(b) shows the imaging results without any range alignment applying 2D FFT to the raw data of a single antenna element.

Next, the proposed eigenspectrum based entropy map (21), the conventional Fourier spectrum-based entropy map (20) and the combination of both entropies (23) are applied to the simulated data and the simulation results are shown in Fig. 6, where all the entropy results are normalised. The local minimum values are detected with the prominence threshold 0.05 and indicated by the white crosses for all the entropy maps. Here to clearly show the local entropy, we made an assumption that the coarse velocity estimations have been obtained which are in the range from -33 m/s to -40 m/s.

Fig. 6(a) shows the proposed entropy map obtained with the eigenspectrum and Fig. 6(b) shows the counterpart of using the Fourier spectrum. Since the eigenspectrum is not very sensitive to the asymmetric coupling terms, the entropy map shows strong thick lines along the acceleration dimension. Although the resolution of the acceleration is low, one can observe that two targets are distinctly resolved in Fig. 6(a) from the velocity domain, while they can hardly be separated in Fig. 6(b). Therefore, the algorithms for multiple targets imaging of the Fourier spectrum-based EM [20], [22] will fail to image the targets separately. The result of using the proposed combination is shown in Fig. 6(c).

One can observe that although the eigenspectrum-based entropy map provides a high resolution on velocity, it yields local minima with poor acceleration estimations. By contrast, the Fourier spectrum-based entropy map has a much higher

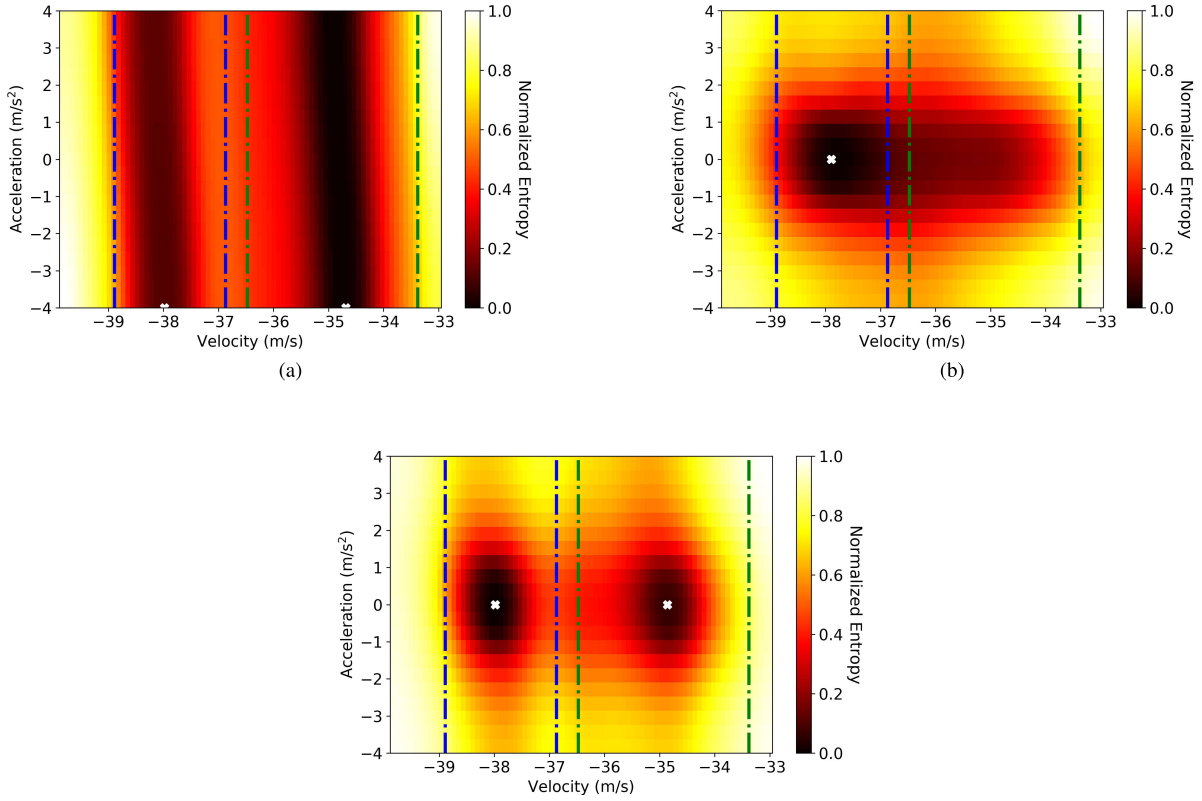

Fig. 6. The entropy map for (a) the eigenspectrum, (b) the Fourier spectrum (c) the Combined entropy by (23).

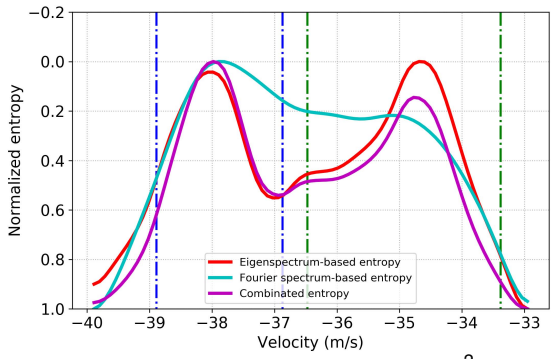

Fig. 7. Entropy maps at slice of $a = 0$ m/s^2.

resolution in the acceleration domain but fails to separate two cars in the velocity. The target detection and motion parameters estimation revealed in Fig. 6(c) by the proposed algorithm are in agreement with the ground truth in terms of velocity and acceleration estimation.

To show the superiority of the proposed algorithm, the entropies at the acceleration 0 m/s^2 are plotted in Fig. 7. There is a deep valley between two peaks which correspond to the cars with the proposed algorithm, while the entropy of the Fourier spectrum is much smoother and only one peak could be recognised.

After the motion parameters estimation, the next step is to image the targets separately. According to (24), the coupling terms are firstly compensated for the phase centre. Secondly, Keystone transform is applied to eliminate the coupling terms for all the scatterers within the unambiguous region. After that, 2D FFT is used to obtain the range-Doppler map of the cars. Finally, the "*shape*" of the targets are extracted using thresholding sequentially.

The two cars are imaged using 2D FFT followed by 10 dB thresholding and the results are shown in Fig. 8. Since two cars are so close in the Doppler velocity domain that it is not possible to separate completely all scatterers and a part of another car would appear in the observed window. The thresholding results are further combined to generate the unfolded range-Doppler map, which is shown in Fig 9. Despite some artifacts, the overall map agrees well to Fig. 4(b).

Then the beamforming results using the algorithm described in Section III-C of two cars are plotted in Fig. 10, where the azimuths of the cars are correctly estimated. In comparison, the beamforming result of using the whole data of the first slow-time is plotted as well, where only one peak can be estimated for a single car.

After estimating the azimuths, the real geometric image can be reconstructed according to the steps proposed in Section III-D and the imaging results are shown in Fig. 11. By comparison with the geometric setting in Fig. 3, the two cars are correctly positioned in the observed scene.

B. Discussions

According to the approximate equation, the far-field antenna beamwidth in degrees of a uniform linear antenna array with L antenna elements and the inter-element spacing equal to the half-wavelength of the electromagnetic field at a center frequency is $112^\circ/(L-1)$. Therefore, for (virtual) uniform linear antenna array with 8 elements in our simulation, the azimuthal resolution is around 16 degrees. However, the angular difference between two maxima corresponding to

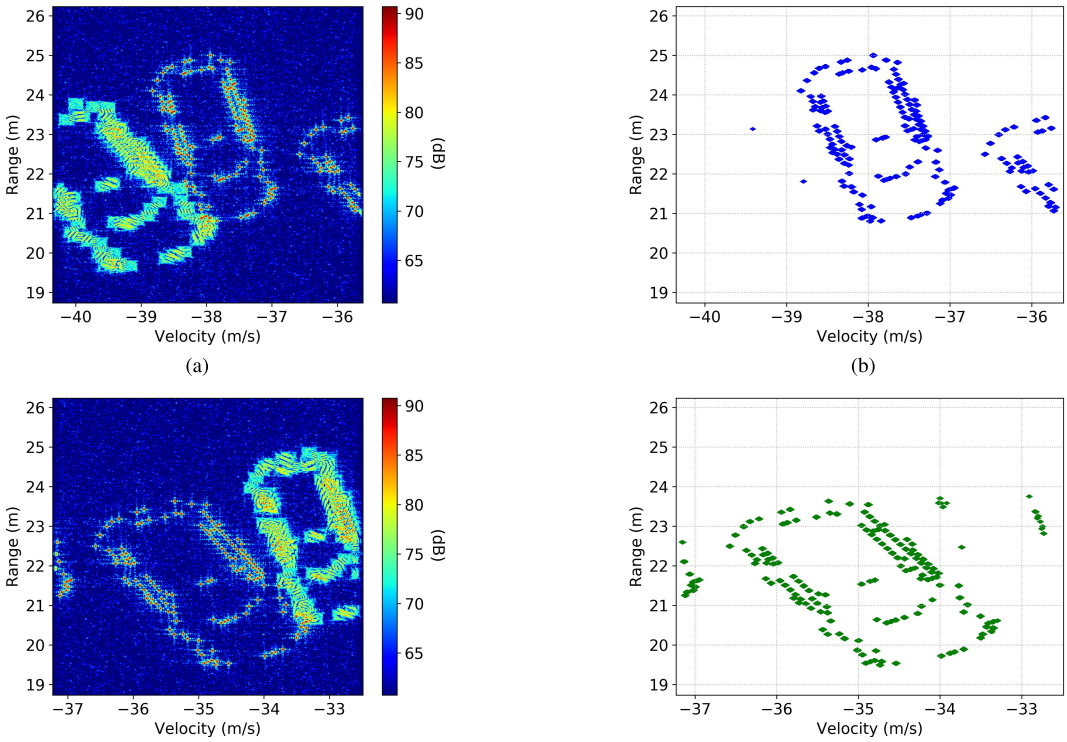

Fig. 8. (a)(b) Focused image and thresholding result for car1 and (c)(d) Focused image and thresholding result for car2.

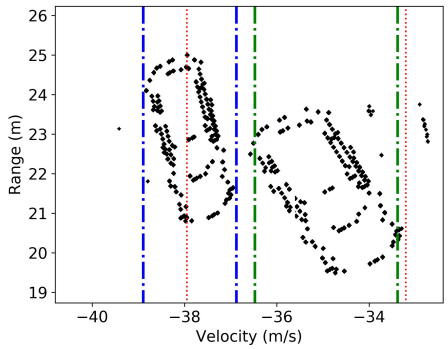

Fig. 9. Estimated unfolded range-Doppler map.

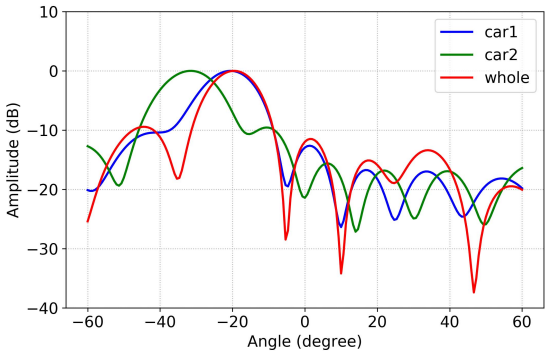

Fig. 10. Beamforming results.

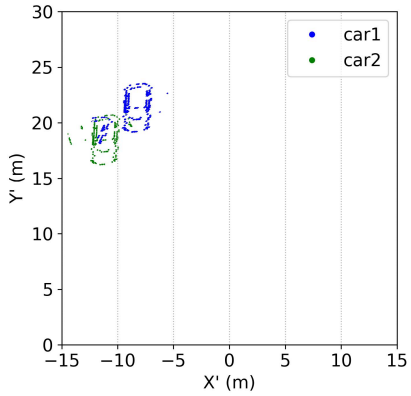

Fig. 11. Reconstructed Scene.

both cars is about 10 degrees, which outperform conventional beamforming. To achieve images with azimuthal resolution similar to those shown in Fig. 10 with conventional beamforming algorithm, the number of antennas in the array should be increased by a factor of ten at least.

In addition to the advantages demonstrated in the simulation, the algorithm has some limitations. The first one is that the eigenspectrum is much easier to be contaminated by the noise than the Fourier spectrum. Therefore, the general performance of the proposed method under low SNR condition, for instance, less than 0 dB, is usually worse than that of Fourier spectrum-based entropy. The second limitation is that the entropy of both eigenspectrum-based and Fourier spectrum-based would fail to separate two targets when their energies of the reflected signals are significantly distinct, for instance, more than 10 dB. The technique presented in this paper, therefore, is more suited to a motorway environment where the targets have similar size and their accelerations are low. However, with more complicated acceleration compensation, the technique is also promising in an agile urban environment. The last limitation is that the eigenspectrum-based algorithm needs much larger computational power than the Fourier spectrum-based one and the time consumptions for them in our simulation are, respectively, around 10 seconds and 5 seconds on the Intel Dual Core i5-4250U. Since the

complexity for eigendecomposition and Fourier transform are $\mathcal{O}(\min(M, K)^3)$ and $\mathcal{O}(MK\log(MK))$, respectively, if both M and K are larger, such time consumption difference would be more significant. However, with the rapid development of computer engineering and the introduction of GPUs in automotive applications, we expect that the hardware will be not a limiting factor for the application of the algorithm proposed in already in nearest future. Despite these limitations, the proposed approach of the combined entropy provides better performance than existing methods.

V. Conclusions

The motion parameters estimation and range-Doppler imaging of multiple moving extended-targets are addressed in this paper. To improve the moving targets separation in the Doppler velocity domain when the targets are moving with almost the same accelerations, a novel auto-focusing method based on the entropy of the eigenspectrum is proposed. Combining the proposed eigenspectrum-based entropy and Fourier spectrum-based entropy, both Doppler velocities and higher-order motion parameters can be estimated accurately. After estimating the motion parameters, the azimuthal values of the extended targets are estimated by reconstructing the corresponding signal model which cannot be separated in the beam profile. Finally, the spatial images of extended targets are reconstructed. The numerical simulation results demonstrate high cross-range resolution capability of the algorithm for moving targets and applicability of the proposed method to the automotive domain. The advantage over the conventional algorithm is demonstrated for moderate SNR condition. The operational limitations of the algorithm are discussed. The general idea of the proposed method does not depend on the transmitted waveform and can be easily generalised to other waveforms.

Acknowledgment

The authors would like to thank China Scholarship Council (CSC) for the funding support for the first author.

References

[1] D. Xiao, F. Su, and J. Wu, "Multi-target ISAR imaging based on image segmentation and short-time Fourier transform," in *Proc. 5th Int. Congr. Image Signal Process.*, Oct. 2012, pp. 1832–1836.

[2] C. Ozdemir, *Inverse Synthetic Aperture Radar Imaging With MATLAB Algorithms*, vol. 210. Hoboken, NJ, USA: Wiley, 2012.

[3] T. Itoh, H. Sueda, and Y. Watanabe, "Motion compensation for ISAR via centroid tracking," *IEEE Trans. Aerosp. Electron. Syst.*, vol. 32, no. 3, pp. 1191–1197, Jul. 1996.

[4] L. Xi, L. Guosui, and J. Ni, "Autofocusing of ISAR images based on entropy minimization," *IEEE Trans. Aerosp. Electron. Syst.*, vol. 35, no. 4, pp. 1240–1252, Oct. 1999.

[5] D. E. Wahl, P. H. Eichel, D. C. Ghiglia, and C. V. Jakowatz, "Phase gradient autofocus-a robust tool for high resolution SAR phase correction," *IEEE Trans. Aerosp. Electron. Syst.*, vol. 30, no. 3, pp. 827–835, Jul. 1994.

[6] M. Martorella, F. Berizzi, and B. Haywood, "Contrast maximisation based technique for 2-D ISAR autofocusing," *IEE Proc. Radar, Sonar Navig.*, vol. 152, no. 4, pp. 253–262, 2005.

[7] J. Munoz-Ferreras, F. Perez-Martinez, and M. Datcu, "Generalisation of inverse synthetic aperture radar autofocusing methods based on the minimisation of the Renyi entropy," *IET Radar, Sonar Navig.*, vol. 4, no. 4, pp. 586–594, 2010.

[8] M.-S. Kang, J.-H. Bae, S.-H. Lee, and K.-T. Kim, "Efficient ISAR autofocus via minimization of Tsallis entropy," *IEEE Trans. Aerosp. Electron. Syst.*, vol. 52, no. 6, pp. 2950–2960, Dec. 2016.

[9] J. Wang, X. Liu, and Z. Zhou, "Minimum-entropy phase adjustment for ISAR," *IEE Proc. Radar, Sonar Navig.*, vol. 151, no. 4, pp. 203–209, 2004.

[10] S. Zhang, Y. Liu, and X. Li, "Fast entropy minimization based autofocusing technique for ISAR imaging," *IEEE Trans. Signal Process.*, vol. 63, no. 13, pp. 3425–3434, Jul. 2015.

[11] X. Bai, F. Zhou, M. Xing, and Z. Bao, "A novel method for imaging of group targets moving in a formation," *IEEE Trans. Geosci. Remote Sens.*, vol. 50, no. 1, pp. 221–231, Jan. 2012.

[12] X. Dong, Y. Zhang, X. Gu, and W. Zhai, "ISAR imaging of multiple targets based on sparse representations," in *Proc. IEEE Int. Conf. Microw., Commun., Antennas Electron. Syst. (COMCAS)*, Nov. 2015, pp. 1–4.

[13] A. Wang, Y. Mao, and Z. Chen, "Imaging of multitargets with ISAR based on the time-frequency distribution," in *Proc. ICASSP. IEEE Int. Conf. Acoust., Speech, Signal Process.*, Apr. 1994, pp. V-173–V-176.

[14] L. Fan, P. Yiming, and H. Shunji, "Multi-target imaging processing algorithms of ISAR based on time-frequency analysis," in *Proc. CIE Int. Conf. Radar*, Oct. 2006, pp. 1–4.

[15] J. Zhao, Y.-Q. Zhang, X. Wang, S. Wang, and F. Shang, "A novel method for ISAR imaging of multiple maneuvering targets," *Prog. Electromagn. Res.*, vol. 81, pp. 43–54, 2019.

[16] Y. Li, Y. Fu, X. Li, and L.-W. Li, "An ISAR imaging method for multiple moving targets based on fractional Fourier transformation," in *Proc. IEEE Radar Conf.*, May 2009, pp. 1–6.

[17] J. Zhao, M. Zhang, X. Wang, and D. Nie, "Parameters estimation and ISAR imaging of multiple maneuvering targets based on an order reduction method for cubic chirps," *J. Electromagn. Waves Appl.*, vol. 31, no. 16, pp. 1658–1675, Nov. 2017.

[18] X. Fu and M. Gao, "ISAR imaging for multiple targets based on randomized Hough transform," in *Proc. Congr. Image Signal Process.*, vol. 5, 2008, pp. 238–241.

[19] K. Yamamoto, M. Iwamoto, T. Fujisaka, and T. Kirimoto, "An ISAR imaging algorithm for multiple targets of different radial velocity," *Electron. Commun. Jpn. (Part I, Commun.)*, vol. 86, no. 7, pp. 1–10, Jul. 2003.

[20] L. Liu, F. Zhou, M. Tao, and Z. Zhang, "A novel method for multi-targets ISAR imaging based on particle swarm optimization and modified CLEAN technique," *IEEE Sensors J.*, vol. 16, no. 1, pp. 97–108, Jan. 2016.

[21] E. Giusti and M. Martorella, "Range Doppler and image autofocusing for FMCW inverse synthetic aperture radar," *IEEE Trans. Aerosp. Electron. Syst.*, vol. 47, no. 4, pp. 2807–2823, Oct. 2011.

[22] J. Zhao, M. Zhang, and X. Wang, "ISAR imaging algorithm of multiple targets with complex motions based on the fractional tap length keystone transform," *IEEE Trans. Aerosp. Electron. Syst.*, vol. 54, no. 1, pp. 64–76, Feb. 2018.

[23] L. Kong, W. Zhang, S. Zhang, and B. Zhou, "Radon transform and the modified envelope correlation method for ISAR imaging of multi-target," in *Proc. IEEE Radar Conf.*, May 2010, pp. 637–641.

[24] G. H. Golub and C. F. Van Loan, *Matrix Computations*, vol. 3. Baltimore, MD, USA: JHU Press, 2012.

[25] T. G. Kolda and B. W. Bader, "Tensor decompositions and applications," *SIAM Rev.*, vol. 51, no. 3, pp. 455–500, Aug. 2009.

[26] P. Swerling, "Probability of detection for fluctuating targets," *IEEE Trans. Inf. Theory*, vol. IT-6, no. 2, pp. 269–308, Apr. 1960.

[27] Y. Li, Y. Fu, X. Li, and L. Le-Wei, "ISAR imaging of multiple targets using particle swarm optimisation-adaptive joint time frequency approach," *IET Signal Process.*, vol. 4, no. 4, pp. 343–351, 2010.

[28] S. Xu, B. J. Kooij, and A. Yarovoy, "Joint Doppler and DOA estimation using (ultra-) wideband FMCW signals," *Signal Process.*, vol. 168, Mar. 2020, Art. no. 107259. [Online]. Available: http://www.sciencedirect.com/science/article/pii/S0165168419303111

[29] M. Nikolova, "An algorithm for total variation minimization and applications," *J. Math. Imag. Vis.*, vol. 20, nos. 1–2, pp. 89–97, Jan. 2004.

[30] K. E. Dungan, C. Austin, J. Nehrbass, and L. C. Potter, "Civilian vehicle radar data domes," *Proc. SPIE*, vol. 7699, Apr. 2010, Art. no. 76990P.

[31] M. Andres, P. Feil, and W. Menzel, "3D-scattering center detection of automotive targets using 77 GHz UWB radar sensors," in *Proc. 6th Eur. Conf. Antennas Propag. (EUCAP)*, Mar. 2012, pp. 3690–3693.